Simulation of crystal and electronic structures of octahedral molybdenum cluster complex compound Cs-2[Mo6Cl14] using various DFT functionals

Norio Saito, Pierric Lemoine, Stéphane Cordier, Takeo Ohsawa, Yoshiki Wada, Fabien Grasset, Jeffrey Scott Cross, Naoki Ohashi

Journal of the Ceramic Society of Japan 125 [10] 753-759 2017 Full paper

Simulation of crystal and electronic structures of octahedral molybdenum cluster complex compound $Cs_2[Mo_6Cl_{14}]$ using various DFT functionals

Norio SAITO[*,,*****], Pierric LEMOINE[****], Stéphane CORDIER[****], Takeo OHSAWA[**,***], Yoshiki WADA[**,*****], Fabien GRASSET[**,***,*****], Jeffrey Scott CROSS[*] and Naoki OHASHI[**,***,*****,******,†]**

[*]Department of Metallurgy and Ceramics Science, Tokyo Institute of Technology, 2–12–1 Ookayama, Meguro, Tokyo 152–8551, Japan
[**]National Institute for Materials Science, 1–1 Namiki, Tsukuba, Ibaraki 305–0044, Japan
[***]NIMS-Saint-Gobain Center of Excellence for Advanced Materials, National Institute for Materials Science, 1–1 Namiki, Tsukuba, Ibaraki 305–0044, Japan
[****]Institut des Sciences Chimiques de Rennes, Unités Mixtes de Recherché 6226, University of Rennes 1, General Leclerc, Rennes 35042, France
[*****]Laboratory for Innovative Key Materials and Structures, Unité Mixte Internationale 3629, National Institute for Materials Science, 1–1 Namiki, Tsukuba, Ibaraki 305–0044, Japan
[******]Materials Research Center for Element Strategy, Tokyo Institute of Technology, 4259 Nagatsuta, Midori-ku, Yokohama 226–8503, Japan

The electronic and structural characteristics of the octahedral molybdenum cluster-based ternary compound, $Cs_2[Mo_6Cl_{14}]$, were investigated based on density functional theory (DFT) and subsequent comparisons with experimentally observed results. The geometry optimization and band structure calculations of $Cs_2[Mo_6Cl_{14}]$ were performed using three standard functionals: local density approximation, Perdew-Burke-Ernzerhof (PBE) as a generalized gradient approximation, and PBE revised for solid compounds (PBEsol). The validity of the calculated results was experimentally examined via X-ray powder diffraction, ultraviolet–visible (UV–vis) diffuse reflection, and X-ray photoemission spectra (XPS) measurements. PBEsol was found to show the best performance in terms of reproducing the experimentally refined lattice structure of the compound. The calculated band gap energy (E_g) was consistent with the value evaluated from the UV–vis measurement. Furthermore, the XPS valence spectrum of the compound was well reproduced by the calculated projected density of state weighted with the photoionization probabilities of Al K_α. Although the spectral shapes simulated using the three functionals were similar, PBEsol reproduced the energy levels of the electronic states of both $[Mo_6Cl_{14}]^{2-}$ and Cs^+ ion with greater consistency. Therefore, it was concluded that PBEsol is the most appropriate functional for DFT calculations of the metal cluster-based lattice system.

Key-words : Metal cluster, Molybdenum, DFT, Electronic structure, XPS

[Received February 23, 2017; Accepted May 10, 2017]

1. Introduction

Transition metal cluster complexes are among the most important materials in the field of coordination chemistry because of their unique coordination structure and characteristic physical and chemical properties inherent to the metal cluster core. In particular, in octahedral metal cluster chemistry, the octahedral molybdenum cluster-based halide complex, i.e., $[Mo_6X^i_8X^a_6]^{2-}$ (X = halogen; i = inner; a = apical) has long been one of the most investigated cluster materials since it was first described in the mid-1800s.[1)] This complex consists of an octahedral core of 6 Mo(II) atoms surrounded by 14 halogen ligands, i.e., 8 face-capping X^i(s) and 6 terminal-capping X^a(s), which exhibit an overall divalent negative charge (**Fig. 1**). Owing to their extremely large size (~1 nm) compared to single nuclear complexes, these cluster complexes have been used as molecular building blocks by association with various inorganic cationic elements and organic molecules.[2)–5)] In addition, substitution of

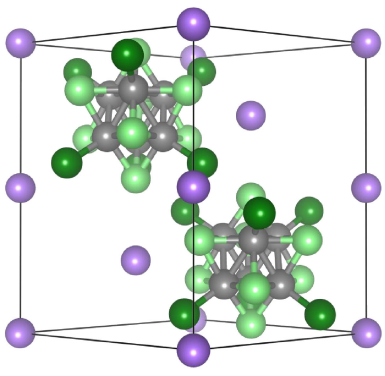

Fig. 1. Representation of the trigonal crystal structure of $Cs_2[Mo_6Cl_{14}]$.

† Corresponding author: N. Ohashi; E-mail: ohashi.Naoki@nims.go.jp
†† Preface for this article: DOI http://doi.org/10.2109/jcersj2.125.P10-1
††† Publication of this international collaborative article is supported by JSPS Grants-in-Aid for Scientific Research (KAKENHI), Grant Number 252016

DOI http://doi.org/10.2109/jcersj2.17039

halogen ligands in other species allows facile fabrication of supramolecular-like highly dimensional and functional nanostructures. For instance, metal organic frameworks (MOFs), such as porous periodical open frameworks[6),7)] and self-assembled cluster monolayers immobilized on the surface of Si(111), have been reported in recent studies on novel electrochemical devices.[8)–10)]

The $[Mo_6X^i_8X^a_6]^{2-}$ complex has attractive chemical and physical properties, such as luminescence,[11),12)] photocatalysis,[13),14)] and redox behavior.[15)] In particular, luminescence is the most attractive property of this complex because of its highly efficient broadband red emission under illumination by UV or blue light.[11),12)] The resultant massive Stokes shift is the most important luminescent characteristic, a potential application of which is the development of red phosphors for solid-state LEDs. In addition, customized optimization of the optical properties is possible, because optical properties such as absorption and luminescence efficiency can be modified according to the chemical composition of the ligands and counter cations.[16)–18)] Thus, understanding the relationship between the composition and the properties of the $[Mo_6X^i_8X^a_6]^{2-}$ complex and the metal-cluster-based solids is crucial for efficient material exploration.

With regard to the relationship between the composition and the properties of the $[Mo_6X^i_8X^a_6]^{2-}$ complex, theoretical studies on the molecular orbitals of the complex have mainly focused on the chloride composition (i.e., $[Mo_6Cl_{14}]^{2-}$)[19)–25)] since around 1980s. However, most of these investigations were performed based on molecular orbital methods using classical Hartree-Fock (HF)-based functionals. Specifically, these studies did not investigate the periodical lattice model in the presence of counter cations. To precisely predict the relationship between the composition and the properties of solids based on the $[Mo_6X^i_8X^a_6]^{2-}$ complex, it is important to conduct investigations based on a crystalline lattice system with counter cations.

With such a background, we have been investigating the crystal structures and electronic properties of $Cs_2[Mo_6X^i_8X^a_6]$ based on density functional theory (DFT) calculations with updated functionals of the exchange–correlation energy. To examine whether DFT is applicable to the metal-cluster-based solid system, we should first determine the most appropriate functional for this system. For this purpose, we attempted to investigate DFT calculations of $Cs_2[Mo_6Cl_{14}]$, which is the most basic composition of the $Cs_2[Mo_6X^i_8X^a_6]$ family, using some standard functionals. Three DFT functionals, i.e., local density approximation (LDA), Perdew-Burke-Ernzerhof (PBE) as a generic generalized gradient approximation (GGA), and PBE revised for solid compounds (PBEsol), were adopted for geometry optimization and band structure calculation of $Cs_2[Mo_6Cl_{14}]$. Among the examined functionals, PBEsol gave lattice parameters nearest to the experimentally determined values. To study the electronic structure, we performed population analyses and projected density of state (PDOS) calculations. Furthermore, to verify the validity of these calculations, we simulated the valence photoemission spectra of $Cs_2[Mo_6Cl_{14}]$ from the calculated PDOS weighted with photoionization probabilities for Al K_α, and subsequently compared them with the observed valence X-ray photoemission spectrum.

2. Materials and methods

2.1 Sample preparation

Synthesis and purification of $Cs_2[Mo_6Cl_{14}]$ were performed according to the procedures reported in the literature.[26),27)] First, $(H_3O)_2[Mo_6Cl_{14}]\cdot 7H_2O$ was prepared as single crystal using a procedure reported by Koknat et al.[28)] Next, $(H_3O)_2[Mo_6Cl_{14}]\cdot 7H_2O$ (10 g, 8.10 mmol) and CsCl (2.75 g, 16.3 mmol) were dissolved separately in ethanol (10 mL), and the obtained solutions were heated until reflux. The CsCl solution was carefully poured into the cluster-dissolved solution under stirring. Subsequently, the obtained solution was evaporated; then, the remaining solid was further re-crystallized after dissolution and filtrated with acetone solution. The powder finally obtained was stored under air at room temperature.

Then, the sample was heated on a hot plate at 150°C for 1 h in a glove box filled with well-dried N_2 gas, where the concentration of water was less than 0.1 ppm. Because the lattice structure of $Cs_2[Mo_6Cl_{14}]$ is highly sensitive to the presence of water molecules absorbed from ambient moisture,[26)] this heat treatment needs to remove the water molecules from the lattice so that the intrinsic nature of the compound can be evaluated.[26)]

2.2 Characterization analysis

The crystal structure of the dried sample was characterized by X-ray powder diffraction (XRD) using a RINT-Ultima III diffractometer (Rigaku Co. Ltd., Tokyo, Japan) with Cu K_α radiation ($\lambda = 0.15418$ nm). The lattice parameters were refined using the least squares method by sampling more than 10 observed diffraction peaks. The diffuse reflectance spectrum of the sample in the near-UV to near-IR range (UV–vis) was measured using a SolidSpec-3700 spectrophotometer (Shimadzu Corp., Tokyo, Japan) with an integrating sphere made of $BaSO_4$. The value of optical band gap (E_g) was determined from the absorption spectrum converted with the Kubelka–Munk (KM) function.[29),30)] The X-ray photoemission spectra (XPS) of the sample in the core-level and valence energy regions were measured using a Σ-probe spectrometer (Thermo Fisher Scientific K.K, Yokohama, Japan) with a monochromated Al K_α X-ray source ($h\nu = 1486.6$ eV). The pass energy was set as 20.0 eV, and the instrumental resolution of electron energy was ~0.2 eV. The sample was attached on an adhesive tape containing carbon particles. When obvious charging under X-ray irradiation occurred, a charge neutralizer employing both Ar^+ ions and electron emitters was used to eliminate the charging. The observed binding energy was calibrated to align the C 1*s* peak of the surface-contaminating carbon to 284.6 eV.

2.3 Computational methods

DFT calculations for $Cs_2[Mo_6Cl_{14}]$ were conducted assuming the trigonal lattice model with the centrosymmetric space group ($P\bar{3}1c$),[2),26),27)] as shown in Fig. 1, because we had previously confirmed the presence of centrosymmetry by observing the absence of second-harmonic generation (SHG) from $Cs_2[Mo_6Cl_{14}]$ under irradiation by a high-intensity infrared (IR) laser.[26)] Hence, relaxation of the lattice parameters and atomic coordinates of $Cs_2[Mo_6Cl_{14}]$ was achieved by applying structural constraints so that the space group of the lattice could maintain the $P\bar{3}1c$ symmetry. The initial structural model for the geometry optimization is summarized in Table S1 in the supporting information.

All the DFT calculations in this study were performed using the plane-wave pseudo-potential method[31)] as implemented in CASTEP code.[32)] The norm-conserving pseudo-potentials (NCPPs)[33)] were generated using OPIUM code.[34),35)] Three exchange–correlation functionals, namely LDA developed by Ceperley and Alder[36)] as reformulated by Perdew and Zunger,[37)] PBE,[38)] and PBEsol,[39)] were employed for energy minimizations using Pulay's density mixing scheme.[40)] The cell parameters and atomic coordinates were relaxed using the quasi-Newton method with the Broyden-Fletcher-Goldfard-Shanno Hessian

update scheme.[41] Electron spin polarization was considered for all DFT calculations. The plane-wave cut-off energy was set at 830 eV, the Monkhorst-Pack grid[42),43)] (4 × 4 × 3 mesh) was employed for Brillouin-zone sampling, and a 96 × 96 × 144 mesh was used for fast Fourier transformation. The convergence tolerances were set to 5×10^{-5} nm for atomic displacement, 5×10^{-6} eV/atom for total energy, 0.1 eV/nm for maximum interatomic force, and 0.02 GPa for pressure. For population analysis, we deduced the effective charge of each element based on two methods, i.e., Mulliken population analysis[44),45)] and Hirshfeld population analysis.[46),47)] To simulate the photoemission spectrum, the calculated PDOS was weighted by some reference photoionization probabilities.[48)]

3. Results and discussion

3.1 Experimental structural characterization

Figure 2 shows the XRD pattern of the synthesized sample. Although the observed pattern was identical to the pattern simulated with the structural parameters of trigonal $Cs_2[Mo_6Cl_{14}]$,[2),49)] some extra peaks were found at 11.14, 14.74, and 15.44°. We have previously reported[26),27)] that these extra peaks are due to the crystallization of $Cs_2[Mo_6Cl_{14}]\cdot H_2O$ together with $Cs_2[Mo_6Cl_{14}]$ during the re-crystallization procedure. Because these diffraction intensities were negligible, we can assume that the sample has a nearly trigonal phase. As indicated in **Table 1**, the refined lattice parameters were $a = 0.9789(1)$ nm, $c = 1.4195(3)$ nm, and $V = 1.1779(1)$ nm^3, which were slightly smaller than the values reported in the literature.[26)] These smaller lattice parameters imply that the volatile constituents, namely water molecules,[26)] were satisfactorily removed from the lattice through the heat treatment at 150°C for 1 h in the glove box. Therefore, the synthesized sample must exhibit the intrinsic structural characteristics of $Cs_2[Mo_6Cl_{14}]$.

3.2 Computational analyses

Although the geometry optimization and energy minimization of $Cs_2[Mo_6Cl_{14}]$ fairly converged for all calculations, the obtained lattice parameters differed significantly with the chosen functional. Among the three functionals, PBEsol gave the lattice parameters nearest to the experimentally obtained values, as indicated in **Table 2**. As can be seen from this table, the lattice parameters optimized by LDA resulted in smaller lattice parameters along the *a*- and *c*-axes compared to the observed values. This result is due to the typical tight binding tendency of LDA.[50),51)] By contrast, in the case of PBE, the lattice parameters were overestimated significantly although overestimation of the lattice parameters by a small percentage is a general tendency of GGA.[50),51)] On the other hand, PBEsol reduced this overestimation considerably, such that the lattice parameter was well matched with the observed one along the *a*-axis albeit somewhat larger along the *c*-axis. The atomic coordinates and interatomic distances resulting from the geometry optimization are summarized in Tables S2 and S3, respectively. These results show that the lengths of the Cs–Cl bonds mainly influenced the variation in the lattice parameters, because the lengths of the Mo–Mo, Mo–Cl^i, and Mo–Cl^a bonds seemed to be comparable to the experimentally refined values[26)] regardless of the functional class. Hence, the selection of an appropriate functional is crucial for reproducing the arrangement of the cluster complexes and counter cations in the metal-cluster-based lattice system. The most accurate lattice structure was obtained using PBEsol, which could be attributed to PBEsol being specifically designed for yielding accurate jellium surface energies.[39),52)] Assuming the $[Mo_6Cl_{14}]^{2-}$ complex as one large anion with high electron density, PBEsol would be appropriate for estimating the surface energy of the cluster complex, which likely leads to adequate ionic positions of the $[Mo_6Cl_{14}]^{2-}$ complexes and Cs^+ ions in the lattice.

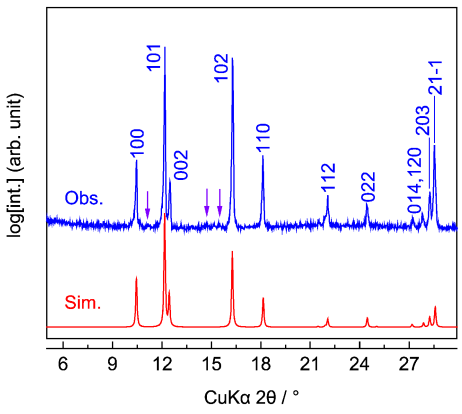

Fig. 2. Observed and simulated XRD pattern of $Cs_2[Mo_6Cl_{14}]$. The arrows in observed profile denote the diffraction peaks of the secondary phase, i.e., $Cs_2[Mo_6Cl_{14}]\cdot H_2O$.

Table 1. Experimentally refined lattice parameters of $Cs_2[Mo_6Cl_{14}]$ in trigonal form and reference values

	Lattice parameters		
	a (nm)	*c* (nm)	*V* (nm^3)
Exp.	0.9789(1)	1.4195(3)	1.1779(1)
Ref.	0.9789(1)	1.4214(2)	1.1796(2)

Figure 3 shows the band structure and total DOS (TDOS) of $Cs_2[Mo_6Cl_{14}]$ calculated with the three functionals. Because the energy band structures for the up- and down-spin states are identical, only the up-spin component is shown in the *E*-*k* dispersion plots, and the TDOS plotted here is the summation of the up- and down-spin components. As can be seen from Fig. 3, each band is very flat over the *k*-space, and the bands with similar energy levels seem to form bundles. These very flat bands indicate strongly localized electron distribution in the lattice, and the bundle-like structure is reflected in the highly degenerated molecular orbitals of the $[Mo_6Cl_{14}]^{2-}$ complex. The calculated band gap energies (E_g) are listed in **Table 3**. They are consistent with the values observed from UV–vis diffuse reflection, as shown in Fig. S1, even though LDA and GGA underestimate E_g values owing to the well-known problem of the self-interaction error.[37),53),54)] This result suggests that effective screening of the metal-cluster-based compounds would be possible by predicting the E_g values without using high-cost exchange–correlation functionals developed for obtaining plausible E_g values, such as hybrid functionals.[55),56)]

The calculated band structures presented in Fig. 3 show that the degree of the *E*-*k* dispersion was obviously different by adopted functional. For instance, band pairs indicated with arrows in Figs. 3(b) and 3(c) are merged to form a broad bundle in Fig. 3(a).

Table 2. Lattice parameters of $Cs_2[Mo_6Cl_{14}]$ resulting from geometry optimization via DFT with three different functionals

	Lattice parameters		
Functional	*a* (nm)	*c* (nm)	*V* (nm^3)
LDA	0.958	1.385	1.101
PBE	1.005	1.582	1.383
PBEsol	0.980	1.475	1.227

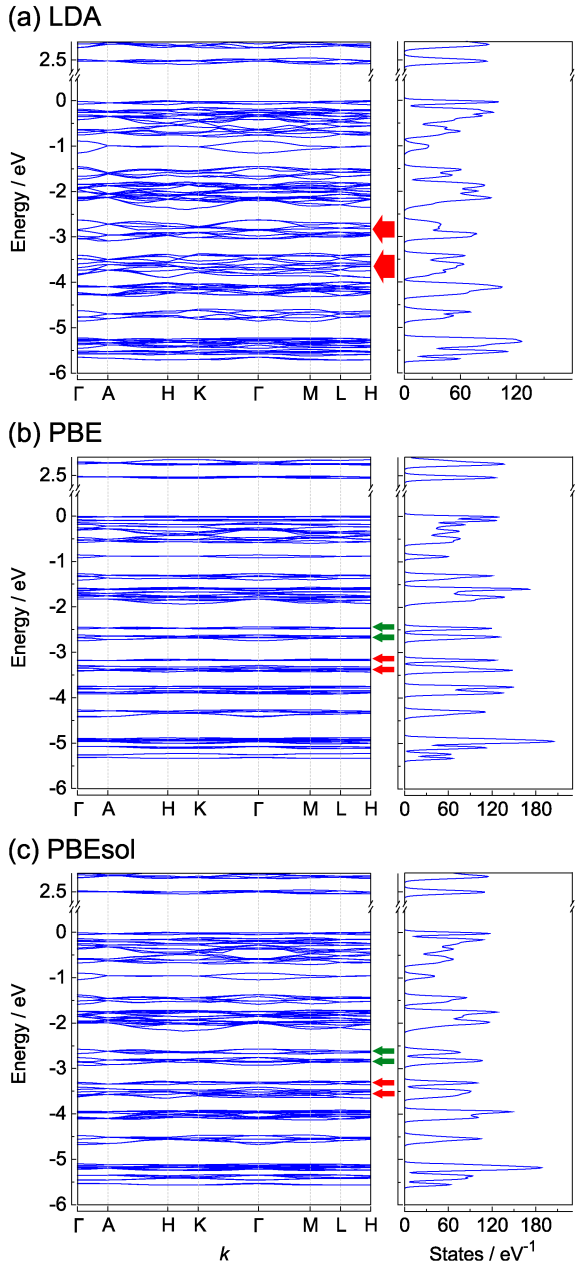

Fig. 3. Energy band structure and total DOS of $Cs_2[Mo_6Cl_{14}]$ calculated with (a) LDA, (b) PBE, and (c) PBEsol functionals. The arrows indicate band pairs classified as a bundle.

Table 3. Energy band gap (E_g) of $Cs_2[Mo_6Cl_{14}]$ determined by optical reflectance measurement and DFT calculations with three different functionals

		E_g (eV)
Exp.		2.6
DFT calc.	Functional	
	LDA	2.43
	PBE	2.45
	PBEsol	2.46

In particular, the width of each bundle in Fig. 3(b) is very narrow for GGA calculation, while it is obviously broad in Fig. 3(a) for LDA calculation. The broader band dispersion of LDA is because LDA systematically assumes constant electron density for a system although the realistic charge distribution is not uniform. In contrast to LDA, PBE and PBEsol yielded relatively flat band structures, but the latter appeared to be slightly dispersed, as shown in Figs. 3(b) and 3(c). Because the band dispersion variation is reflected in the different bonding states of the lattice system, we will now discuss the details of the chemical state of each element through PDOS and effective charge studies.

The PDOS of $Cs_2[Mo_6Cl_{14}]$ is shown in **Fig. 4**. In this figure, the valence band maximum (VBM) of $Cs_2[Mo_6Cl_{14}]$ is found to be mainly composed of the Mo 4*d* orbitals, and the Mo 4*d* and Cl 3*p* orbitals dominate the entire valence band (VB). The contribution of Cl is nearly separated into Cl^i and Cl^a at the boundary near −3.0 eV, suggesting significantly different chemical states of both elements. Indeed, as shown in Fig. S2, the XPS spectrum of $Cs_2[Mo_6Cl_{14}]$ in the Cl 2*p* region confirmed that it could be separated into two doublets peaks, and the ratio of both spectral areas was identical to the ratio of Cl^a/Cl^i ($6/8 = 0.75$). This result obviously indicates a chemical shift of Cl^i and Cl^a. Because the PDOS of Cl^i is located in a deeper energy range than that of Cl^a, Cl^i and Mo are more strongly hybridized. Moreover, the hybridization degree between Mo and Cl was likely changed by the functional, as the valence band width of the Mo 4*d* orbitals became broader in the order of LDA > PBEsol > PBE. With regard to the Cs 5*p* orbitals, they were located away from the VB region by a few electron volts, indicating electronic localization of the Cs^+ ion and $[Mo_6Cl_{14}]^{2-}$ complex. The energy level of the Cs 5*p* orbitals decreased in the order of PBE < PBEsol < LDA. This variation reflects a slight change in the ionicity of the Cs^+ ion according to these functionals.

To provide a better understanding of the chemical states of these elements, the results of Mulliken and Hirshfeld effective charge analyses are shown in **Table 4**. It can be seen that the performances of both the population methods were consistent, although the Hirshfeld method was likely to give smaller values. As described above, the nature of Cl^a is ionic, which is supported by the strong negative charge of Cl^a. The charge of Cl^i was nearly neutral even though the Cl atom is negatively charged in general, owing to the charge compensation for the strong electronic hybridization between Cl^i and Mo. Although LDA and PBEsol gave close charge values with respect to Mo, Cl^i, and Cl^a, PBE gave more ionic ones. This result indicates that PBE tends to localize Mo and Cl compared to LDA and PBEsol. The charge value of the Cs^+ ion was nearly the same as the formal charge regardless of employed functional in the Mulliken analysis. However, in the Hirshfeld analysis, it seemed to enhance the ionicity in the order of PBE > PBEsol > LDA. This tendency is consistent with the dependency of the *E*-*k* dispersion in Fig. 3. Indeed, the energy band structure calculated with LDA showed the broadest dispersion while that calculated with PBE showed the narrowest dispersion. The difference in these band dispersions was well reflected in the degree of covalency represented by the results of charge analyses. As the metal-cluster-based system is composed of many boding nature, such as metallic bond within the Mo_6-core, relatively strong covalency in Mo–Cl^i bonds and ionic bonding character in Mo–Cl^a bonds, effectiveness of charge analysis based on PDOS calculation seems to be very limited. However, it seems that the Hirshfeld analysis is rather better way for semi-quantitative expression of the bonding characteristics as described above. It is also noteworthy that simple electrostatic charge model, so-called bond valence sum,[57] is not appropriate for analysis of bonding characteristics in metal-cluster-based compounds.[58] We attribute this difficulty in electrostatic charge analysis to coexistence of many different kinds of bonds, like

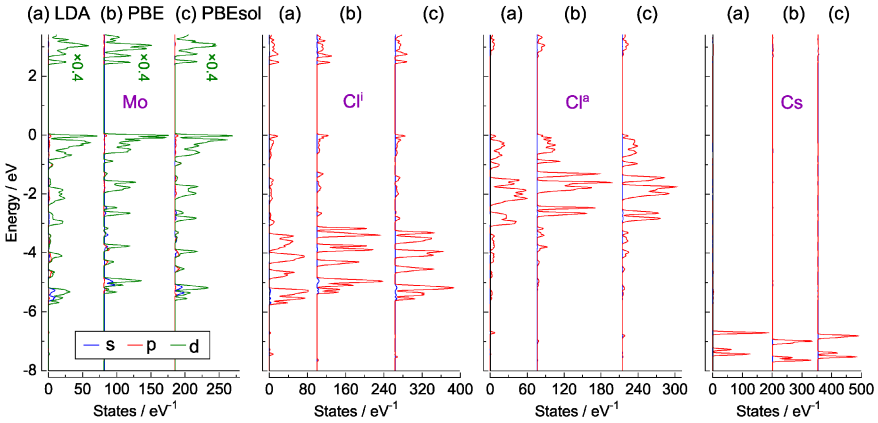

Fig. 4. PDOS of $Cs_2[Mo_6Cl_{14}]$ calculated with (a) LDA, (b) PBE, and (c) PBEsol functionals.

Table 4. Effective ionic charge in $Cs_2[Mo_6Cl_{14}]$ calculated by Hirshfeld and Mulliken analysis for the results of DFT calculations with three different functionals

Functional	Mo	Cl^i	Cl^a	Cs
Mulliken effective charge (/*e*)				
LDA	0.17	−0.07	−0.39	0.95
PBE	0.29	−0.14	−0.43	0.97
PBEsol	0.20	−0.08	−0.40	0.97
Hirshfeld effective charge (/*e*)				
LDA	0.15	0.01	−0.22	0.18
PBE	0.18	−0.01	−0.26	0.27
PBEsol	0.15	0.01	−0.24	0.22

metallic and ionic bonds, within a metal cluster complex. In other words, DFT calculation for periodic lattice system must be appropriate for description of the chemical bonds formed in the metal cluster complex.

3.3 Simulation of valence XPS spectra

We simulated the photoemission spectrum of $Cs_2[Mo_6Cl_{14}]$ in the valence band region from the calculated PDOS shown in Fig. 4 to examine the accuracy of the calculated electronic structure of the compound. In this simulation, each PDOS was multiplied by the photoionization probabilities[48] for Al K_α listed in Table S4, and they were finally combined into one spectrum. **Figure 5** shows a comparison between the experimentally observed and simulated XPS spectra. For the first impression, agreement between the observation and simulation seems to be not very good. In fact, the width of valence band in the observation was approximately 1.0 eV wider than that in the simulation, although spectral shapes in the observed and calculated spectra looked similar to each other.

There are two major reasons for disagreement between simulation and observation. One reason is that spin–orbit coupling (SOC) was not considered in simulations. This results in difference in number of peaks in valence band between observation and simulations. In fact, there are five major peaks in simulated spectra as denoted by arrows in the figure but six in observation. As seen in the reference,[59] Cs 5*p* level splits into two XPS peaks, 5*p* 3/2 at ∼12.3 eV and 5*p* 1/2 at ∼14.0 eV, due to the SOC. On the other hand, Cs 5*p* forms single peak in simulated spectra because the SOC was not taken into account. Hence, peak splitting due to the SOC is one of the reasons why the observed spectra showed relatively wider valence band spectra.

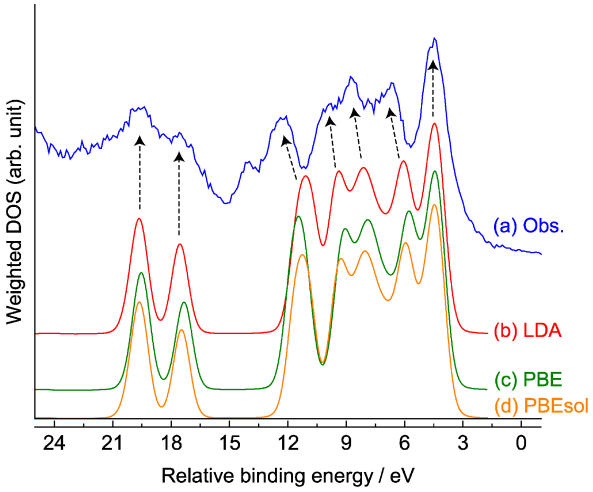

Fig. 5. XPS valence band spectra of $Cs_2[Mo_6Cl_{14}]$: (a) observation, simulation with (b) LDA, (c) PBE, and (d) PBEsol functionals.

The other reason for the difference in width of the valence band between observed and simulated spectra was essentially caused by a commonly known habit in DFT simulations. That is narrowing of valence band width by self-interaction[54),60] which is significantly found in *d*-electron system.[61),62] Usage of hybrid functional method with non-local potential is a possible way to reproduce experimental valence band width[63),64] but 10–100 times more computational costs should be also expected for simulation using the hybrid functional compared to the DFT functional applied to this study. As the valence band spectrum calculated using PBEsol showed rather better similarity (relative peak intervals) with observation and the band width was calculated so as to be rather wider by using PBEsol, we may conclude that the similarity of observation and calculation was improved by employing PBEsol. Considering the overall reproducibility of the lattice structure as well as computational costs, we concluded that PBEsol is appropriate for crystal and band structure calculations of the metal-cluster-based compound system.

4. Conclusions

In summary, we synthesized $Cs_2[Mo_6Cl_{14}]$ and investigated its crystal and electronic structures through comparisons between experimental investigations and theoretical predictions using the DFT method. To determine the most appropriate functional for this lattice system, three DFT functionals, namely LDA, PBE,

and PBEsol, were adopted for geometry optimization and band structure calculations of the compound. A comparison between the calculated and experimentally refined lattice structures indicated that PBEsol is the most accurate functional. The results of the band energy calculations showed that DFT could give the band gap energy of $Cs_2[Mo_6Cl_{14}]$ observed from UV–vis absorption measurements within an error of a few electron volts. Furthermore, a comparison between the observed and simulated XPS spectra in the valence energy region indicated that the simulation reproduced the major spectral characteristics of the observed spectrum. Although LDA and PBE misestimated the energy levels of the electronic states with respect to the Cs^+ ion and the $[Mo_6Cl_{14}]$ complex, respectively, PBEsol predicted the precise energy range for both the states. Considering the overall results of the lattice structure studies, we conclude that PBEsol is the most appropriate functional for DFT calculations of the $Cs_2[Mo_6Cl_{14}]$ lattice system.

Acknowledgement This work was carried out as part of the France-Japan international collaboration framework (UMI 3629-LINK Center). The authors wish to thank the people involved in LINK and related activities, particularly Dr. David Lechevalier, Dr. Mari Kono, and Dr. Benjamin Dierre of Saint-Gobain KK (Tokyo, Japan), as well as Noée Dumait and Serge Paofai of ISCR for their contributions to the synthesis of metal cluster precursors. N.S. would also like to thank Prof. Junzo Tanaka of Tokyo Tech for support and encouragement. The study was financially supported by Saint-Gobain (France), CNRS, Université de Rennes 1, and NIMS through LINK UMI 3629, with additional contributions from Region Bretagne (France) and Fondation Langlois.

References

1) W. Blomstrand, *J. Prakt. Chem.*, **77**, 88–119 (1859).
2) M. Potel, C. Perrin, A. Perrin and M. Sergent, *Mater. Res. Bull.*, **21**, 1239–1245 (1986).
3) K. Kirakci, S. Cordier and C. Perrin, *Z. Anorg. Allg. Chem.*, **631**, 411–416 (2005).
4) G. Saito, H. Hosoda, Y. Yoshida, J. Hagiwara, K. Nishimura, H. Yamochi, A. Otsuka, T. Hiramatsu, Y. Shimazaki, K. Kirakci, S. Cordier and C. Perrin, *J. Mater. Chem.*, **22**, 19774–19791 (2012).
5) W. Preetz, K. Harder, H. G. V. Schnering, G. Kliche and K. Peters, *J. Alloy. Compd.*, **183**, 413–429 (1992).
6) R. L. Bain, D. F. Shriver and D. E. Ellis, *Inorg. Chim. Acta*, **325**, 171–174 (2001).
7) D. Bůžek, J. Hynek, M. Kučeráková, K. Kirakci, J. Demel and K. Lang, *Eur. J. Inorg. Chem.*, **28**, 4668–4673 (2016).
8) S. Ababou-Girard, S. Cordier, B. Fabre, Y. Molard and C. Perrin, *ChemPhysChem*, **8**, 2086–2090 (2007).
9) B. Fabre, S. Cordier, Y. Molard, C. Perrin, S. Ababou-Girard and C. Godet, *J. Phys. Chem. C*, **113**, 17437–17446 (2009).
10) S. Cordier, B. Fabre, Y. Molard, A.-B. Fadjie-Djomkam, P. Turban, S. Tricot, S. Ababou-Girard and C. Godet, *J. Phys. Chem. C*, **120**, 2324–2334 (2016).
11) A. W. Maverick and H. B. Gray, *J. Am. Chem. Soc.*, **103**, 1298–1300 (1981).
12) A. W. Maverick, J. S. Najdzionek, D. MacKenzie, D. G. Nocera and H. B. Gray, *J. Am. Chem. Soc.*, **105**, 1878–1882 (1983).
13) P. Kumar, S. Kumar, S. Cordier, S. Paofai, R. Boukherroub and S. L. Jain, *RSC Advances*, **4**, 10420–10423 (2014).
14) A. Barras, S. Cordier and R. Boukherroub, *Appl. Catal., B-Environ.*, **123–124**, 1–8 (2012).
15) H. B. Gray and A. W. Maverick, *Science*, **214**, 1201–1205 (1981).
16) T. C. Zietlow, M. D. Hopkins and H. B. Gray, *J. Solid State Chem.*, **57**, 112–119 (1985).
17) F. Grasset, F. Dorson, S. Cordier, Y. Molard, C. Perrin, A.-M. Marie, T. Sasaki, H. Haneda, Y. Bando and M. Mortier, *Adv. Mater.*, **20**, 143–148 (2008).
18) K. Kirakci, K. Fejfarová, M. Kučeráková and K. Lang, *Eur. J. Inorg. Chem.*, **14**, 2331–2336 (2014).
19) H. Honda, T. Noro and K. Tanaka, *J. Chem. Phys.*, **114**, 10791–10797 (2001).
20) H. Imoto and T. Saito, *Inorg. Chem.*, **34**, 2415–2422 (1995).
21) L. M. Robinson, R. L. Bain, D. F. Shriver and D. E. Ellis, *Inorg. Chem.*, **34**, 5588–5596 (1995).
22) Z. Lin and I. D. Williams, *Polyhedron*, **15**, 3277–3287 (1996).
23) F. A. Cotton and G. G. Stanley, *Chem. Phys. Lett.*, **58**, 450–453 (1978).
24) R. Ramirez-Tagle and R. Arratia-Pérez, *Chem. Phys. Lett.*, **460**, 438–441 (2008).
25) K. Costuas, A. Garreau, A. Bulou, B. Fontaine, J. Cuny, R. Gautier, M. Mortier, Y. Molard, J.-L. Duvail, E. Faulques and S. Cordier, *Phys. Chem. Chem. Phys.*, **17**, 28574–28585 (2015).
26) N. Saito, Y. Wada, P. Lemoine, S. Cordier, F. Grasset, T. Ohsawa, N. Saito, J. Cross and N. Ohashi, *Jpn. J. Appl. Phys.*, **55**, 075502 (2016).
27) N. Saito, P. Lemoine, N. Dumait, M. Amela-Cortes, S. Paofai, T. Roisnel, V. Nassif, F. Grasset, Y. Wada, N. Ohashi and S. Cordier, *J. Clust. Sci.*, **28**, 773–798 (2017).
28) F. W. Koknat, T. J. Adaway, S. I. Erzerum and S. Syed, *Inorg. Nucl. Chem. Lett.*, **16**, 307–310 (1980).
29) W. W. Wendlandt and H. G. Hecht, "Reflectance Spectroscopy", Interscience Pub., New York (1966).
30) S. P. Tandon and J. P. Gupta, *Phys. Status Solidi*, **38**, 363–367 (1970).
31) V. Milman, B. Winkler, J. A. White, C. J. Pickard, M. C. Payne, E. V. Akhmatskaya and R. H. Nobes, *Int. J. Quantum Chem.*, **77**, 895–910 (2000).
32) S. J. Clark, M. D. Segall, C. J. Pickard, P. J. Hasnip, M. J. Probert, K. Refson and M. C. Payne, *Z. Kristallogr.*, **220**, 567–570 (2005).
33) D. R. Hamann, M. Schlüter and C. Chiang, *Phys. Rev. Lett.*, **43**, 1494–1497 (1979).
34) D. R. Hamann, *Phys. Rev. B*, **40**, 2980–2987 (1989).
35) A. W. Rappe, K. M. Rabe, E. Kaxiras and J. D. Joannopoulos, *Phys. Rev. B*, **41**, 1227–1230 (1990).
36) D. M. Ceperley and B. J. Alder, *Phys. Rev. Lett.*, **45**, 566–569 (1980).
37) J. P. Perdew and A. Zunger, *Phys. Rev. B*, **23**, 5048–5079 (1981).
38) J. P. Perdew, K. Burke and M. Ernzerhof, *Phys. Rev. Lett.*, **77**, 3865–3868 (1996).
39) J. P. Perdew, A. Ruzsinszky, L. G. I. Csonka, O. A. Vydrov, G. E. Scuseria, L. A. Constantin, X. Zhou and K. Burke, *Phys. Rev. Lett.*, **100**, 136406 (2008).
40) P. Pulay, *Chem. Phys. Lett.*, **73**, 393–397 (1980).
41) B. G. Pfrommer, M. Côté, S. G. Louie and M. L. Cohen, *J. Comput. Phys.*, **131**, 233–240 (1997).
42) H. J. Monkhorst and J. D. Pack, *Phys. Rev. B*, **13**, 5188–5192 (1976).
43) J. D. Pack and H. J. Monkhorst, *Phys. Rev. B*, **15**, 1748–1749 (1977).
44) M. D. Segall, R. Shah, C. J. Pickard and M. C. Payne, *Phys. Rev. B*, **54**, 16317–16320 (1996).
45) M. D. Segall, P. J. D. Lindan, M. J. Probert, C. J. Pickard, P. J. Hasnip, S. J. Clark and M. C. Payne, *J. Phys.: Condens. Matter*, **14**, 2717–2744 (2002).
46) F. L. Hirshfeld, *Theor. Chim. Acta*, **44**, 129–138 (1977).
47) K. B. Wiberg and P. R. Rablen, *J. Comput. Chem.*, **14**, 1504–1518 (1993).
48) J. H. Scofield, *J. Electron Spectrosc.*, **8**, 129–137 (1976).
49) Pearson's Crystal Data ASM International, Ohio, 2014, No.

1928748.
50) G. I. Csonka, J. P. Perdew, A. Ruzsinszky, P. H. T. Philipsen, S. Lebègue, J. Paier, O. A. Vydrov and J. G. Ángyán, *Phys. Rev. B*, **79**, 155107 (2009).
51) P. Haas, F. Tran and P. Blaha, *Phys. Rev. B*, **79**, 085104 (2009).
52) Y. Zhao and D. G. Truhlar, *J. Chem. Phys.*, **128**, 184109 (2008).
53) J. Heyd, J. E. Peralta, G. E. Scuseria and R. L. Martin, *J. Chem. Phys.*, **123**, 174101 (2005).
54) A. J. Cohen, P. Mori-Sánchez and W. Yang, *Chem. Rev.*, **112**, 289–320 (2012).
55) J. Paiera, M. Marsman, K. Hummer, G. Kresse, I. C. Gerber and J. G. Ángyán, *J. Chem. Phys.*, **124**, 154709 (2006).
56) M. V. Schilfgaarde, T. Kotani and S. V. Faleev, *Phys. Rev. B*, **74**, 245125 (2006).
57) D. Xue and X. He, *Phys. Rev. B*, **73**, 064113 (2006).
58) E. Levi and D. Aurbach, *Chem. Mater.*, **23**, 1901–1914 (2011).
59) G. S. Zakharova, N. V. Podval'naya and M. V. Kuznetsov, *Russ. J. Inorg. Chem.*, **56**, 267–272 (2011).
60) T. Schmidt and S. Kümmel, *Computation*, **4**, 33 (2016).
61) J. J. Mudd, T.-L. Lee, V. Muñoz-Sanjosé, J. Zúñiga-Pérez, D. J. Payne, R. G. Egdell and C. F. McConville, *Phys. Rev. B*, **89**, 165305 (2014).
62) I. Suzuki, H. Nagatani, M. Kita, Y. Iguchi, C. Sato, H. Yanagi, N. Ohashi and T. Omata, *Inorg. Chem.*, **55**, 7610–7616 (2016).
63) F. Oba, A. Togo and I. Tanaka, *Phys. Rev. B*, **77**, 245202 (2008).
64) T. Ohsawa, S. Ueda, M. Suzuki, Y. Tateyama, J. R. Williams and N. Ohashi, *Appl. Phys. Lett.*, **107**, 171604 (2015).